Journal of Electronic Materials (2024) 53:4956–4968
https://doi.org/10.1007/s11664-024-11047-3

28TH INTERNATIONAL CONFERENCE ON NUCLEAR TRACKS AND RADIATION MEASUREMENTS

Study of Thermal Behavior and Activation Energy of Various Polymer Nanocomposite Blend Membranes

Harsh D. Patel[1] · **Naveen K. Acharya**[1]

Received: 7 December 2023 / Accepted: 12 March 2024 / Published online: 10 April 2024

Abstract

The solution casting method was used to synthesize nanocomposites of polymethyl methacrylate (PMMA) and polystyrene (PS) polymer with graphene oxide (GO). It was determined that the conductivity of the PS/GO and PMMA/GO polymer nanocomposites was ionic and electronic, respectively. The thermal conductivity of the nanocomposites was investigated with regard to the impact of crystallinity and free volume. This paper reports a differential scanning calorimetric (DSC) study of PMMA/GO (1%) and PS/GO (1%) and nanocomposite blends of PMMA and PS prepared in different ratios by weight percentage of PMMA/PS (80:20, 60:40, 50:50, 60:40, 20:80) with 1% of GO using the solution casting method. The samples were analyzed using a DSC instrument at heating rates of 5°C/min, 10°C/min, and 20°C/min in the temperature range of 50–160°C. Fourier transform infrared (FTIR) spectroscopy and x-ray diffraction (XRD) studies of the blends showed that the crystalline phases of PS and PMMA depended on the GO percentage in the composite solutions. Significant shifts were seen in FTIR, XRD, and DSC analyses, and DSC and TGA thermograms of the nanocomposite blend confirmed the formation of a PS/PMMA blend and demonstrated a significant change in thermal behavior with the blend ratio. The activation of the pure and blended polymers was determined through their glass transition using different isoconversional methods.

Graphical Abstract

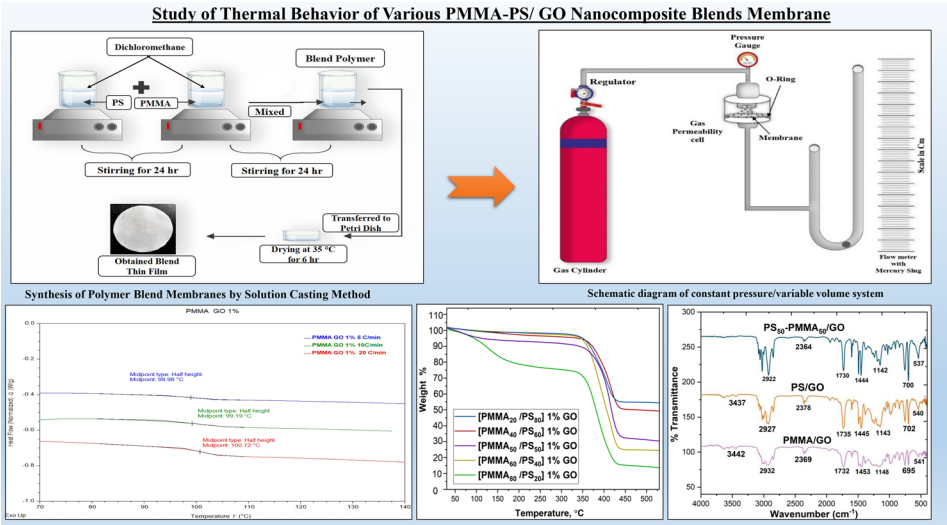

Keywords Graphene oxide nanofiller · polymer nanocomposite blends · differential scanning calorimetry · glass transition temperature (T_g)

Extended author information available on the last page of the article

Introduction

Polymer nanocomposites have emerged as an area of great interest in the field of polymer nanotechnology because of their wide range of technical and industrial uses. In contrast to the bulk polymer matrix, polymer nanocomposites display radically distinct behavior. This is because nano-sized fillers have superior properties as a result of their increased surface area. Polymeric materials can be made conductive by adding nanoparticles that interact with their conjugated bonds. Polymer conductivity can be improved by many orders of magnitude by adding conducting nanofillers at the correct concentration. The incorporation of nanofillers improves the electrical characteristics of the polymer matrix by introducing layers of conductive nanofillers into the matrix. The most critical aspect for improving the electrical performance of nanocomposites is the creation of an interface between the polymeric chains and the nanofillers. The thermal characteristics of polymer nanocomposites can also be improved through the addition of inorganic/organic nanofillers.[1] Multifunctional polymer nanocomposites may be prepared using graphene oxide (GO) with a two-dimensional structure. The exceptional electrochemical characteristics of GO nanoparticles are widely acknowledged. The conductivity of polymer nanocomposites may be improved by adding GO nanofillers to the insulating polymeric matrix. Supercapacitors and solar cells are just a few of the many applications of graphene-related materials that are currently under development. Polystyrene (PS) also has a high degree of thermal stability compared to other polymers. As an alternative to polystyrene, polymethyl methacrylate (PMMA) is an excellent choice. Styrene-based materials have unique properties due to their molecular structure, including long-term durability, excellent performance, and design flexibility.

In this study, we examined how crystallinity and activation energy affect the thermal conductivity of PS/GO and PMMA/GO polymer nanocomposites. Pure PMMA, PS, and a nanocomposite blend of PMMA-PS containing 1 wt.% GO were investigated. The amphiphilic character of polar polymers like PMMA and PS helps in the dispersion of GO nanofillers in the matrix. Despite this, the creation of large aggregates makes it challenging to disperse GO in polymer matrices; surface alteration is a systematic approach used to prevent this issue. Adding an ionic liquid to the surface may promote dispersion and compatibility with the matrix; it is possible to create miscible or immiscible polymer blends with chemical components and composites that vary in shape by taking advantage of this phase behavior.[3] The phase behavior of a polymeric material may be determined using its glass transition temperature (T_g); when the polymer structure reaches this temperature, it becomes rigid, brittle, and glassy, but beyond this threshold, it stays soft and viscous. The T_g of a polymeric material determines both its production temperature and its end-use qualities, and it may be used it to explore thermodynamic parameters such as specific heat capacity (SHC), glass transition temperature (T_g), and other kinetic features. It is possible to determine the melting and transition points of polymers using differential scanning calorimetry (DSC) thermal analysis.[1–3] Glass transition temperatures and DSC tests show a decrease in the projected melting point (T_m), which is dependent on the molecular weight of the polymer, suggesting likely polymer breakdown. In other words, poorer-quality polymers are more prone to melt at lower temperatures than higher-quality polymers. This parameter may also be used to determine the quantity of a particular polymer or nanofillers in a solution.[4] When a new solvent is introduced into a polymer mix, a phenomenon known as crystallization occurs.[5] Mixing requires negative Gibbs free energy, which may be expressed as interaction energy, combinatorial entropy, and compressibility. For a miscible polymer mix to be stable, its second derivative must be positive.

DSC uses a high-tech instrument designed to detect energy directly, and to accurately estimate heat capacity; heat flow differences between samples and the reference can be measured using DSC, which can then determine how much heat has been taken up or evacuated. This method is based on the idea that when a sample is subjected to a physical change like a phase transition and must retain the same temperature, more or less heat must flow than in the reference. Regardless of whether the method is successful endothermically or exothermically, the kind of process determines the amount of heat that needs to flow to the sample. When heated using DSC, polymer structures become rubbery or viscous at the T_g, which is the point when the polymer structure becomes elastic; cooling amorphous polymers to this temperature results in the transformation of their glassy characteristics into those of a more brittle, stiff, and rigid nature, and these polymers can be identified at this temperature.[6] The chemical composition of the polymer and the mobility of the polymeric chains determine the temperature range for most synthetic polymers; amorphous polymers are distinct from crystallized polymers. Amorphous polymers have T_g, whereas crystalline polymers have T_g and T_m; T_g is visible in both polymers. For breaking to occur, a polymer must undergo a phase transition from a glassy to a rubbery state.[7] DSC and differential thermal analysis (DTA) may be employed to assess various materials, including amorphous and semicrystalline varieties. Exothermic and endothermic transition peaks are provided by thermal analysis techniques

used by DSC and DTA, which help detect phase shifts and thermal changes. An amorphous solid glass transition peak is seen when the material's temperature has risen to a certain level. Polymeric materials' phase behavior may be determined by measuring their glass transition temperature (T_g). Above this temperature, polymeric materials are soft and fluid; below it, they are complex, brittle, and glassy.[3,8] This study employs two amorphous polymers, PMMA and PS. However, the study of the many processes of blends and layered structures is still in its infancy. Polymer–polymer interfaces in pure and mixed samples were thus of particular interest.[4,5] According to the polymer science literature, many scientists have focused on measurement of the glass transition temperature, phase morphology, thermal characteristics, and mechanical capabilities of polymeric blends, in addition to other features.[9,10] Knowledge of their thermal properties is essential to achieving a cost-effective and energy-efficient mix in activity involving semiconductor chips, laser applications, and other high-energy devices. Because interactions between polymeric phases are energetically unfavorable, this system contains multiple steps and interphases. The properties of polymer blends are closely associated with their morphology and phase separation. Polymer scientists are increasingly interested in studying the glass transition temperature and morphological analyses, thermal properties, and mechanical properties.[11,12]

Theory

Many approaches have been devised to analyze the crystallization process, which consists of two main events: nucleation and growth. Most approaches use the Kolmogorov–Johnson–Mehl–Avrami (KJMA) transformation rate equation.[13,14] This equation is obtained through isothermal tests and it is written as

$$\frac{d\alpha}{dt} = nK(1-\alpha)[-\ln(1-\alpha)]^{(1-n)/n} \quad (1)$$

where α is the Avrami exponent (also known as growth exponent), and K is the rate constant in the form of Arrhenius temperature at a particular time t. The regular rate, $K(T)$, is calculated as follows:

$$K(T) = k_0 \exp\left(\frac{-E}{RT}\right) \quad (2)$$

The energy needed to start an exponential process is known as the activation energy (E), while the universal gas constant R is a constant that applies to all gases.

The KJMA rate equation, based on many fundamental assumptions, seems valid for reactions related to linear growth under varying conditions.[15] Estimating the activation energy (E) is not the only metric required to comprehend the whole scenario of crystallization kinetics; microstructural data obtained throughout the transformation is also crucial. In this context, isokinetic and isoconversional approaches may help with crystallization kinetics.

Experimental Setup

Synthesis of Nanocomposite Blend Membranes

In comparison to the polymer matrix phase, which was easily soluble, graphene oxide nanoparticles dissolved in the same or a different solution.[16] Using the solution casting technique, the mixture of polymeric films made of PMMA and PS with nanofillers of graphene oxide was developed. All the composite blend films were dissolved in dichloromethane using a glass plate magnetic stirrer, and composites of PMMA/GO (1%), PS/GO (1%), and PMMA-PS composite with GO (1%) were prepared. Using a probe-sonicator, PS (80:20, 60:40, 50:50, 60:40, and 20:80) was sonicated for 1 h and then stirred again for 24 h at room temperature.[13,17]

Characterization of Membrane Films

Differential Scanning Calorimetry (DSC) Analysis

Thermal analysis and determination of the pure and blended polymer glass transition temperature were carried out using a DSC-25 (TA Instruments, USA) system. The DSC analysis of the PMMA/GO (1%), PS/GO (1%), and composite blend of PMMA-PS/GO (1%) films made with various blending wt.% ratios is presented in this work.[18] The DSC test depicts the miscibility behavior of polymer blends and composites by monitoring the glass transition temperature for all blend ratios utilized for PMMA/PS (80:20, 60:40, 50:50, 60:40, and 20:80) with 1% graphene oxide. Amorphous components in the composite significantly affect the T_g of the semicrystalline domains in the composite, according to the findings of this study. Here, we scanned film with different heating rates of 5°C/min, 10°C/min, and 20°C/min with an accuracy of ± 1°C. The sample was heated to 160°C at 5°C/min for the first scan and then cooled to 40°C for the second scan, which was used to clear the last scan's thermal history, and the same experiment was performed with heating rates of 10°C/min and 20°C/min. Heat flow from 50°C to 160°C at heating rates of 5°C/min, 10°C/min, and 20°C/min in a nitrogen environment was used to analyze the samples. Glass transition temperatures and heat capacities were calculated using TRIOS software. During

the DSC experiments, polymer film samples weighing 2.5 mg and 3.8 mg (PS/GO and PMMA/GO, and composite blends of PS-PMMA/GO) in weight percent ratios of 80:20, 60:40, 50:50 and 40:60, 20:80 were utilized. The samples were tested at least three or four times, each time with a different heating rate.

Thermogravimetric Analysis (TGA)

The thermal weight changes were calculated using a TGA-55 (TA Instruments, Dayalbugh, Agra, India). The term "thermal analysis" generally refers to any test that measures the resulting chemical, physical, and structural changes in a material due to heating or cooling. In theory, the temperature is a universal state variable influencing various physical and chemical processes.[18] Thermal analysis, in its broadest sense, refers to any method used in science or technology to characterize a material by changing another variable, usually temperature.

Fourier Transform Infrared (FTIR) Studies

To obtain the FTIR spectroscopic data, a Bruker ALPHA II small FTIR spectrometer was used, using a personal computer (PC) and software provided by GIRDA (Vadodara, India). The FTIR spectra were obtained at room temperature across the wavenumber range of 4200–500 cm^{-1}.[7,10]

Results and Discussion

PMMA/GO, PS/GO, and PMMA-PS/GO nanocomposite blends were synthesized by the solution casting method. The DSC thermograms showed the T_g values of all nanocomposite blends with different heating rates. Here, the value of glass transition for the PMMA/GO composite is 98.98°C at a heating rate of 5°C /min, and for 10°C/min and 20°C/min, the values are 99.19°C and 100.72°C, respectively. The T_g value for the composite of PS/GO is 92.81°C for 5°C/min, 93.57°C for 10°C/min, and 95.57°C for 20°C/min. For the nanocomposite blend of PS_{50}-$PMMA_{50}$ with graphene oxide, the glass transition value is 91.89°C for 5°C/min, 95.34°C for 10°C/min, and 96.16°C for 20°C/min. According to these observations, all of the PS/PMMA (80:20), PS/PMMA (50:50), and PS/PMMA (40:60) blends are miscible while in equilibrium. These results are shown in Figs. 1, 2, and 3.[19] Because of the addition of graphene oxide, blended nanocomposite polymer membranes have a higher glass transition than pure and blended polymer membranes. These phenomena happened because of a decrease in fractional free volume.

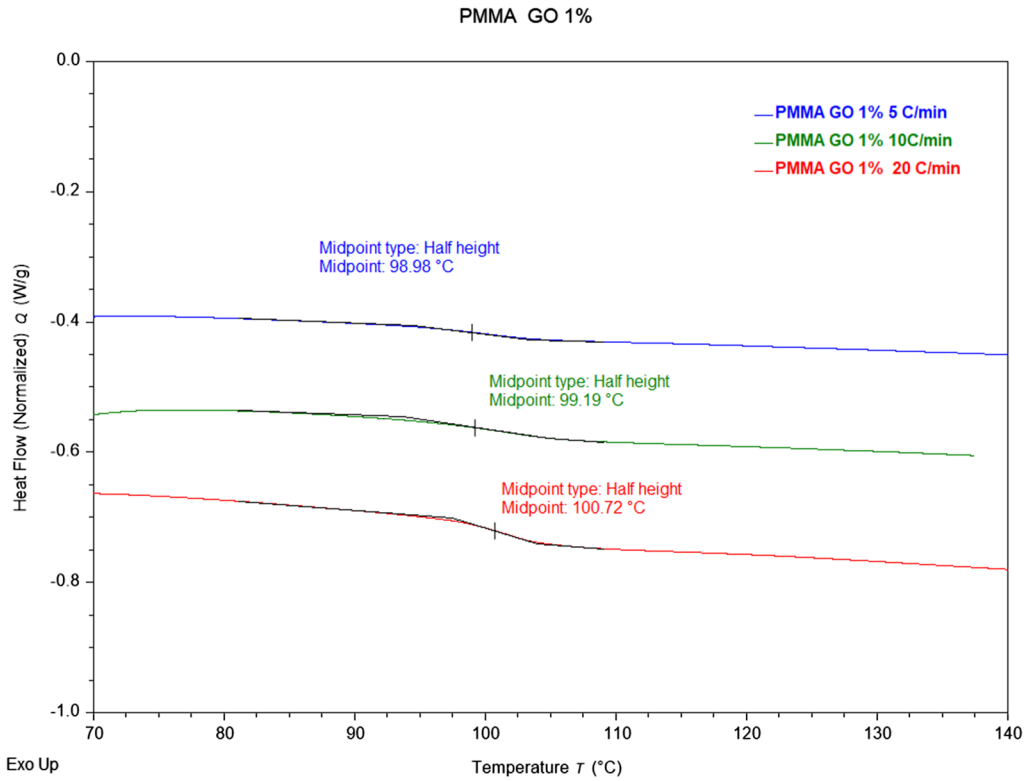

Fig. 1 DSC thermogram of nanocomposite of PMMA/GO polymer membrane.

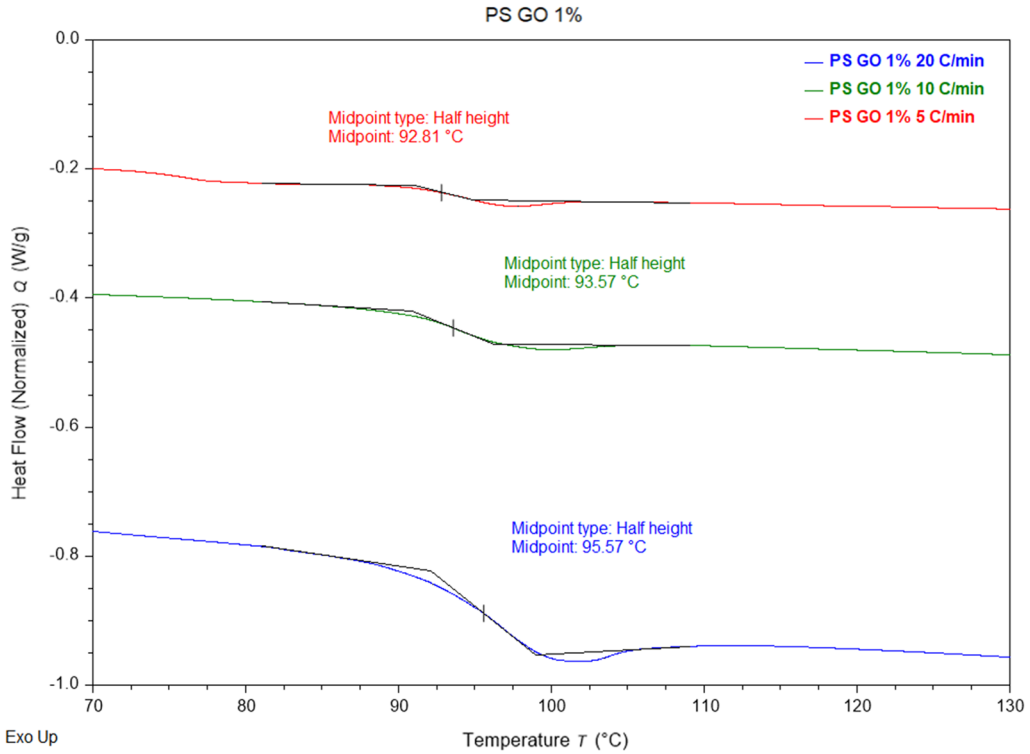

Fig. 2 DSC thermogram of nanocomposite of PS/GO polymer membrane.

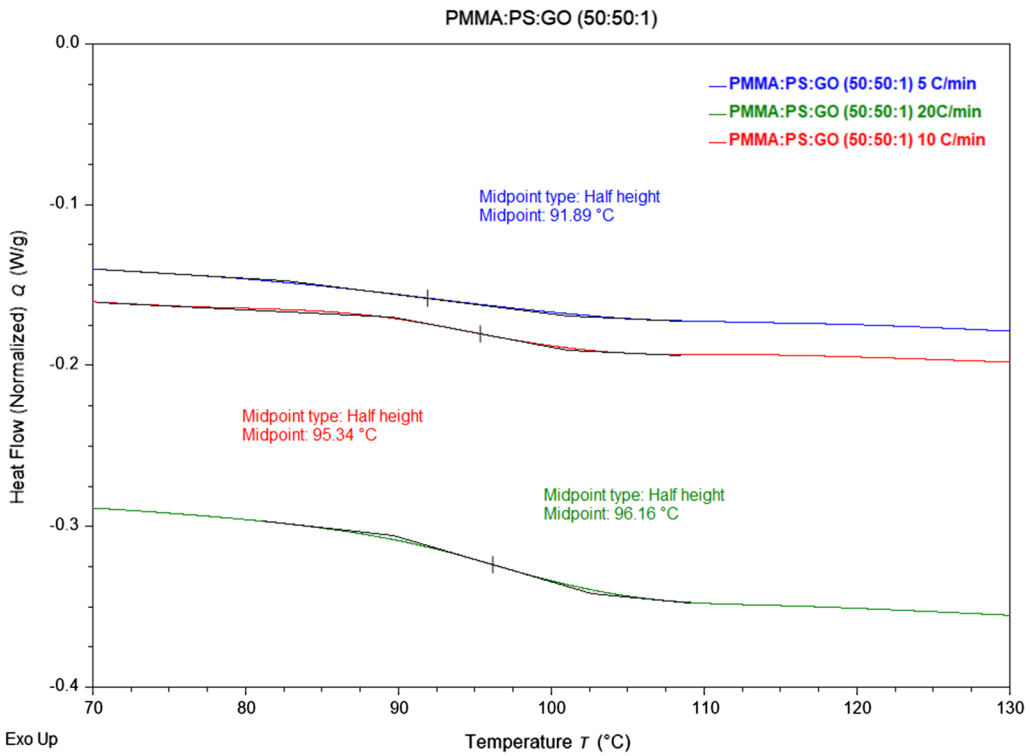

Fig. 3 DSC thermogram of nanocomposite blend of PS-PMMA/GO polymer membrane.

Figures 1, 2, and 3 show the wt.% (weight percentage) values for pure polymer and the different weight ratios of polymer blends of PS/PMMA composite with graphene oxide. Furthermore, DSC was conducted to examine the impact of PMMA in PMMA/PS blends with various concentrations on the T_g value.[19,20] Figures 2 and 3 show the T_g values of pure PS and PMMA polymer with different heating rates, and the graphs indicate that when the heating rate was increased from 5°C/min to 20°C/min, the glass transition temperature also increased according to the heating rate. The T_g values of the PS/PMMA-GO composite blend are shown in Fig. 3. It can be seen that the T_g changed with the change in the wt.% ratios of miscible polymer blends, because of the miscible bonding between PS and PMMA polymer.[14] Here, graphene oxide plays a significant role in the composite and pure polymers with graphene oxide, where the glass transition increased compared to the pure polymer and PS and PMMA polymer blends,[18] due to the functional groups in graphene, including the epoxide, carboxyl, and hydroxyl groups.

The values of T_g were obtained from the DSC thermogram using TRIOS software and are presented in Table I. For the nanocomposite blend thin film with a $PMMA_{50}$-PS_{50} / GO ratio, the experimental value of T_g is around 95.34°C. Hence, these results confirm the observed behavior of the heterogeneous polymeric systems.[21–25]

Isoconversional Methods

Activation energy values obtained by isoconversional techniques are accurate. These techniques may be broken down into two groups: differential and integral. The fundamental kinetic equation serves as the foundation for all isoconversional methods.[1,2]

$$\frac{d\alpha}{dt} = K(T)f(\alpha) \tag{3}$$

Here $K(T)$ is the rate constant from Eq. 2, and $f(\alpha)$ is the KJMA-formalized model of the reaction (Eq. 1). Integral expressions for Eq. 3 are as follows:

$$g(\alpha) = \int_0^{\alpha} [f(\alpha)]^{-1} d\alpha = \frac{k_0}{\beta} \int_0^{T} \exp\left(\frac{-E}{RT}\right) dT \tag{4}$$

Due to the unavailability of the exact solution of the temperature integral in the above Eq. 4, several approximations have been made, which resulted in different methods. The most commonly used methods have been discussed in this paper to calculate the kinetic parameters.[3,4]

Approaches to Isoconversion Based on Linear Integrals

Ozawa–Flynn–Wall (OFW) Method

To simplify the temperature integral in Eq. 4, Ozawa, Flynn, and Wall employed an estimate proposed by Doyle in their technique. The expression denotes the OFW technique:

$$\ln \beta = -1.0516 \frac{E_\alpha}{RT_\alpha} + \text{const.} \tag{5}$$

The slope of $\ln(\beta)$ versus $1/T_\alpha$ yields $-1.0516\,\frac{E_\alpha}{R}$, which may be used to compute the activation energy. The same may be said for $T = T_p$ (Ozawa method).

In Fig. 4 we can find the activation energy using the OFW plot. The activation energy of pure PS/GO is 157.88 E/kJ mol^{-1} and for PMMA/GO is 485.53 E/kJ mol^{-1}.[26,27] When we increased the wt.% of PMMA in the PMMA-PS/GO nanocomposite blends, the activation energy increased higher than that of PS but not above the activation energy of PMMA. This is because of the miscible and glassy behavior of both polymers and the presence

Table I Comparison of T_g values of nanocomposite blend membranes from the DSC experimental results

Variation in temp. RAMP rate	Pure PS	Pure PMMA	PS + 1% GO	PMMA + 1% GO	$PMMA_{80}$/ PS_{20} + 1% GO	$PMMA_{60}$/ PS_{40} + 1% GO	$PMMA_{50}$/ PS_{50} + 1% GO	$PMMA_{60}$/ PS_{40} + 1% GO	$PMMA_{20}$ / PS_{80} + 1% GO
T_g (°C) Ramp rate of 5°C/min	90.23	97.17	92.81	98.98	98.5	96.75	91.89	94.25	94.52
T_g (°C) Ramp rate of 10°C/min	90.77	97.22	93.57	99.19	98.8	97.59	95.34	95.45	94.96
T_g (°C) Ramp rate of 15°C/min	90.70	97.6	95.57	100.72	100.96	100.89	96.16	95.82	95.12

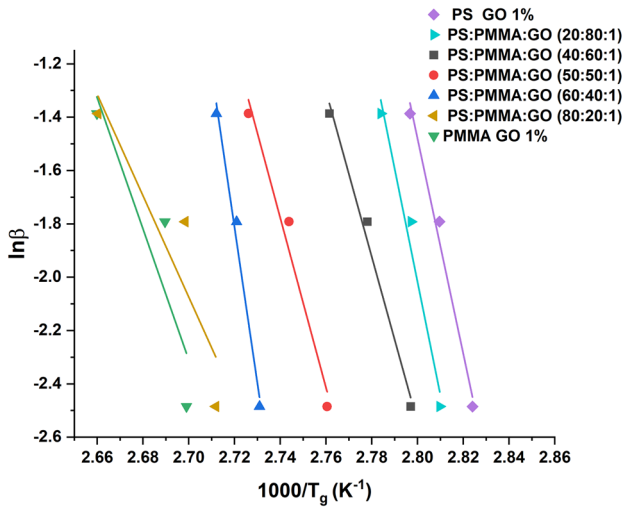

Fig. 4 Ozawa–Flynn–Wall (OFW) plot of nanocomposite blends of PMMA-PS/GO.

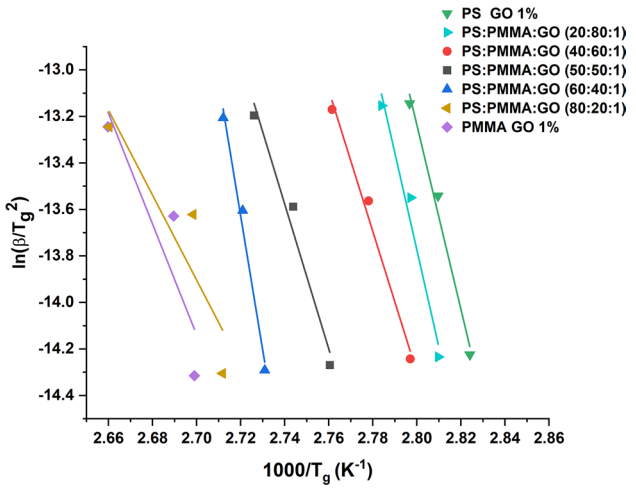

Fig. 5 Kissinger–Akahira–Sunose (KAS) plot of nanocomposite blends of PMMA-PS/GO.

of graphene oxide. In comparison to pure polymers and polymer blends, the activation energy increases when graphene oxide is added.

Kissinger–Akahira–Sunose (KAS) Method

Because the precise solution of the temperature integral in Eq. 4 is not available, Coats and Redfern[5] provided an estimate in their paper that employed the KAS technique. This approach yields the following expression:

$$\ln\left(\frac{\beta}{T^2}\right) = -\frac{E}{RT} + \ln\left(\frac{k_0 R}{Eg(\alpha)}\right) \tag{6}$$

The E values are determined by the slope of the plot $\ln(\beta/T_2)$ versus $1/T$ for constant conversion. The following are some of the KAS method's exceptional cases:

Kissinger Method

This method[19] implies that the degree of conversion (α) is constant at the peak temperature (T_p) when the reaction rate is most important. The Kissinger formula is as follows:

$$\ln\left(\frac{\beta}{T_P^2}\right) = -\frac{E}{RT_P} + \ln\left(\frac{k_0 R}{E}\right) \tag{7}$$

As shown in Fig. 5, the activation energy was calculated on the Kissinger–Akahira–Sunose (KAS) plot for PMMA/GO, which was is found to be 479.46 E/kJ mol^{-1}, and for pure PS it was 151.73 E/kJ mol^{-1}. The activation energy values increased as we increased the PMMA weight percentage in the PMMA-PS/GO nanocomposites. Moreover, from this plot, we can also observe that as we go from PS/GO to PMMA/GO, the value of the intercept slope also increases; for PS/GO its value is 18.25, and for PMMA/GO it is 57.67.[28–30] Here, because of its composite with GO, the activation energy drastically increased compared to pure and polymer blends. This graph shows that OFW and KAS results are near one another, but Friedman's points are much more dispersed.

Boswell Method

As suggested by Boswell,[6,7] the following equation may be used to determine the activation energy at the peak temperature (T_p):

$$\ln\left(\frac{\beta}{T_P}\right) = -\frac{E}{RT_P} + \text{const.} \tag{8}$$

From the plot of Fig. 6 of Boswell for the membranes, we calculated the activation energy for PS/GO, PMMA/GO, and blended composite of $PMMA_{50}$-PS_{50}/GO. The value of activation energy (AE) is 155.47 E/kJ mol^{-1} for PS/GO, and the slope is 18.7. For PMMA/GO, the AE value is 347.27 E/kJ mol^{-1}, and the slope is 57.4. For $PMMA_{50}$-PS_{50}/GO, the AE value is 260.24 E/kJ mol^{-1}, and the slope is 30.5.[31]

Augis and Bennett's Method

Augis and Bennett[32] indicated that this approach might be used for heterogeneous processes given by the Avrami expression in Eq. 7 as an extension of the Kissinger method. The onset temperature of crystallization (T_0) is combined with the peak crystallization temperature in this approach, yielding correct E values from the following equation:

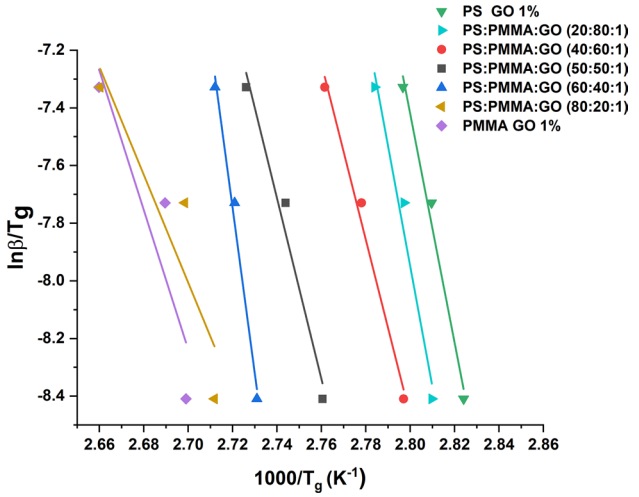

Fig. 6 Boswell plot of PS/GO, PMMA/GO, and nanocomposite blends of PMMA-PS/GO polymer membranes.

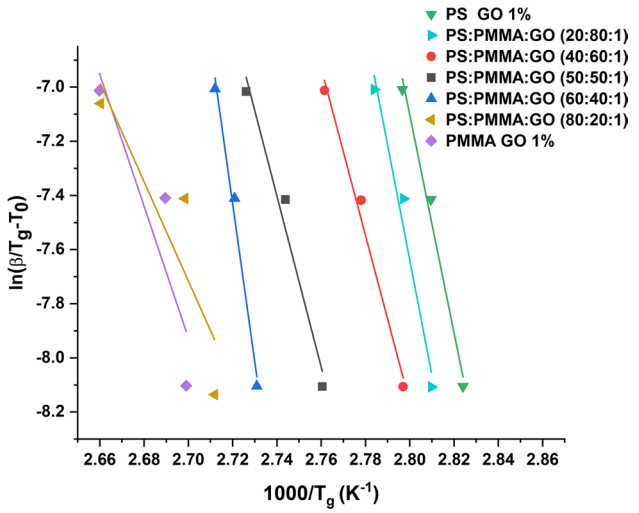

Fig. 7 Augis and Bennett's plot of PS/GO, PMMA/GO, and nanocomposite blends of PMMA-PS/GO polymer membranes.

$$\ln\left(\frac{\beta}{T_P - T_0}\right) = -\frac{E}{RT_P} + \ln k_0 \tag{9}$$

Here, in Fig. 7 the activation energy was calculated from Augis and Bennett's plot for pure PMMA/GO, which showed a value of 485.62 E/kJ mol^{-1}, and for pure PS/GO it is 152.31 E/kJ mol^{-1}. Increasing the weight percentage of PMMA in the PMMA-PS/GO blends improved the activation energy value.[33] Moreover, from this plot, we can also observe that as we go from PS/GO to PMMA/GO, the value of the intercept slope also increases for PS/GO; its value is 18.3, and for PMMA/GO it is 58.4.

Table II presents the activation energy of the nanocomposite blends of PS-PMMA/GO calculated from isoconversional method plots. The non-isothermal crystallization kinetics of the present glassy polymer may thus be studied using Augis and Bennett's method. The kinetics of crystallization were examined using both isokinetic and isoconversional approaches. The isoconversion method may be used to calculate the activation energy and the pre-exponential factor (k_0), because it does not use any mathematical approximation to simplify the temperature integral in Eq. 4. This approach of linear differential isoconversion is believed to yield accurate estimates of the activation energy. As a result, no assumptions about the reaction model are required.[16,34] This indicates that the approach is unaffected by the reaction model. The example that follows shows a particular situation of the Friedman method where the activation energy could be calculated:

$$\ln\left(\beta\frac{\mathrm{d}\alpha}{\mathrm{d}T_p}\right) = -\frac{E}{RT_p} + \text{const.} \tag{10}$$

TGA

TGA of polymer thermal decomposition has often been used to determine the kinetic parameters, including activation energy. TGA thermograms showing weight loss versus temperature are shown in Fig. 8 for different nanocomposite

Table II Activation energy of nanocomposite blends of PMMA-PS/GO calculated from isoconversional method plots

Method	PS + 1% GO	PMMA + 1% GO	$PMMA_{80}$/PS_{20} + 1% GO	$PMMA_{60}$/PS_{40} + 1% GO	$PMMA_{50}$/PS_{50} + 1% GO	$PMMA_{60}$/PS_{40} + 1% GO	$PMMA_{20}$ / PS_{80} + 1% GO
	E/kJ mol^{-1}						
Ozawa	157.88	485.53	352.49	335.46	264.71	258.14	204.10
Kissinger	151.73	479.46	346.94	329.56	258.64	252.16	197.94
Boswell	155.47	477.77	347.27	330.06	260.24	253.99	200.94
Augis and Bennett	152.31	485.62	352.36	334.86	262.55	256.98	202.19

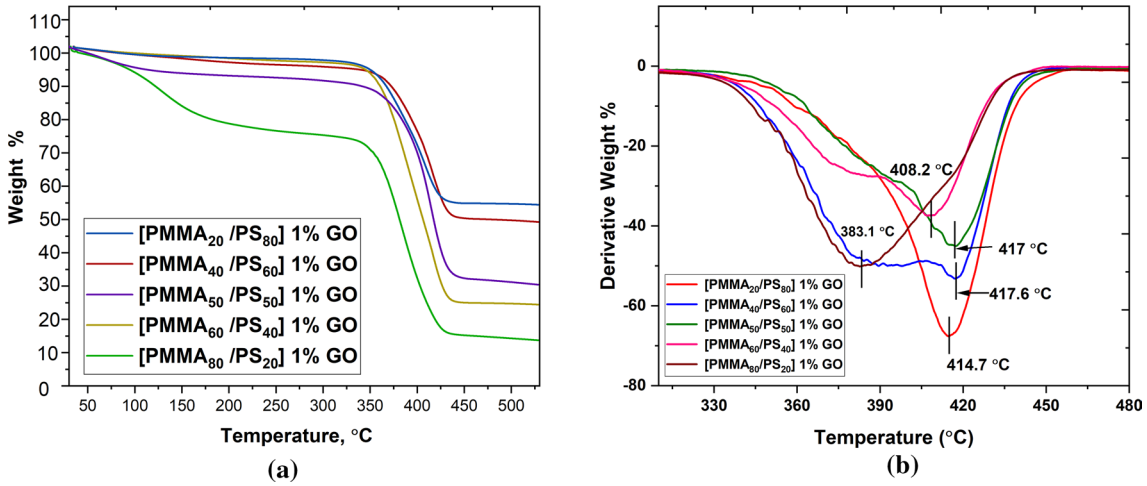

Fig. 8 (a) Thermogravimetric analysis (TGA). (b) Curves of differential thermal analysis (DTA) of various nanocomposite blends of PMMA-PS/GO (1%).

blends of PMMA-PS/GO with varied weight ratios of PMMA and PS, in addition to all the thermal curves of different samples observed at a heating rate of 5°C/min, between 50°C and 600°C. At temperatures between 80°C and 110°C, moisture evaporation causes the first weight loss in all samples; after reaching 130°C, the samples become unstable owing to evaporation of the solvent. All samples show the most significant weight loss at decomposition temperatures (T_d) between 340°C and 430°C.[33,35] At the temperature of 340°C, about 90% of the material is degraded. The process of weight loss and the evaporation of degradation products increases during this phase. When temperatures exceed 400°C, weight loss of roughly 6–7% occurs.

These observations could be related to the structural breakdown of the polymer mixtures. Figure 8 shows the TGA curves of the nanocomposite blend membrane films, which indicate that adding GO nanoparticles to the PMMA/PS blend increases the material's thermal stability. PMMA's thermal degradation is primarily due to the breakdown of C–C bonds, which proceeds through the decomposition of head–head bonds, the breakage of vinyl groups at the polymer's ends, and the random breaking of polymeric chains. Two different phases of weight reduction for the nanocomposites are shown in the thermogram.[36] Initial processing involves solvent removal and polymer end degradation. At this point, graphene oxide contributes to the polymer's increased stability. The weight loss percentage is more significant in the second stage, when the polymer chain is broken down. This is due to the impact of GO nanofillers. The heating has a good influence on thermal stability, as seen by the increase in char percentage. According to the findings, the amount of the inorganic component injected affects how much strength is increased. The addition of the inorganic component greatly decreases the thermal breakdown of PMMA polymer.

Table III The decomposition temperatures of nanocomposite blends of PMMA-PS/GO at different weight loss percentages

Nanocomposite	Stage 1 (%)	Stage 2 (%)	T_{max} (°C)
[$PMMA_{20}/PS_{80}$] 1% GO	4.70	92.30	414.7
[$PMMA_{40}/PS_{60}$] 1% GO	4.55	97.01	417.6
[$PMMA_{50}/PS_{50}$] 1% GO	4.60	98.60	417.0
[$PMMA_{60}/PS_{40}$] 1% GO	8.62	93.45	408.2
[$PMMA_{80}/PS_{20}$] 1% GO	38.40	105.55	383.1

The PMMA/PS blend had a much greater weight loss ratio overall relative to the performance of comparable nanocomposites. Based on the data in Table III, it was determined that the polymer chains and inorganic particles affect the nature of material; thus, PMMA and PS polymer matrix breakdown caused by heat was decreased.[37] The results show that the T_d of pure PMMA and PS polymers has shifted towards higher values due to the increasing weight percentage of PMMA and the addition of graphene oxide nanoparticles to the polymer matrix, compared with pure PMMA, PS, and PMMA-PS blend. There is significant weight loss in stages 1 and 2 for the [$PMMA_{80}/PS_{20}$] 1% GO samples, because of the higher weight percentage of PMMA polymer compared to PS polymer, and due to more C–C bonds breaking; therefore, more fractional free volume is created. An important peak in the DTG curve occurs around 414.7°C. The DTG curve rapidly increases in temperature to a peak at 383.1°C. This is the link in the chain where the breaking apart of polymers into monomers and smaller building blocks such as dimers, trimers, tetramers, and pentamers occurs.[35]

FTIR Analysis

Figure 9 shows that FTIR spectroscopy is an excellent approach for identifying the chemical interactions between filler functional groups and the polymer carbonyl group. Each individual polymer will not recognize a mix of two incompatible polymers in infrared spectrum terms. However, if the polymers are compatible, the infrared spectra of the blend and those of the individual components should vary significantly.[38]

Chemical interactions produce band shifts and broadening, explaining these differences. FTIR spectroscopy was used in this work to further understand the chemical interactions between GO nanoparticles and the PS and PMMA polymer matrix. In Fig. 9, the FTIR spectrum shows the characteristics of blends of nanocomposite PS/GO and PMMA/GO. The spectrum indicates the development of additional peaks at 1730, 1735, and 1732 cm^{-1} for C=O stretching. Peaks are seen at 1444 cm^{-1}, 1445 cm^{-1}, and 1453 cm^{-1} for C–H bending, and 1142 cm^{-1}, 1143 cm^{-1}, and 1148 cm^{-1} for C–O stretching, all of which support the synthesis of PMMA/GO. A broad band can be seen between 2927 cm^{-1} and 2922 cm^{-1} in the spectrum of pure PS. In the spectrum of the composite of graphene and polystyrene, the reactive

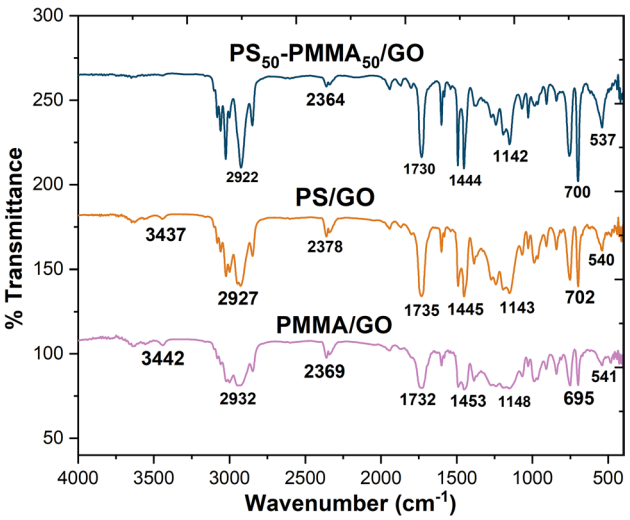

Fig. 9 FTIR spectra of nanocomposites of PS-PMMA/GO.

graphene components collide with the polystyrene's surface, leading to the development of a graphene-based functional group on the surface.[33,35] Polymer etching occurs when atomic graphene interacts with the surface carbon atom to produce volatile reaction products. In contrast, the creation of graphene oxide functional groups at the polymer surface occurs when plasma-activated species interact with the surface carbon atoms.[35]

Due to the presence of GO hydroxyl groups, O–H bond tension vibration at 3437 cm^{-1} and 3443 cm^{-1} is accompanied by a C–OH band at 1445 cm^{-1} and 1453 cm^{-1} in the case of PS/GO and PMMA/GO. The graphene ring's polycyclic aromatic double bonds have a distinctive tension band of C=C at 2364 cm^{-1}, 2378 cm^{-1}, and 2369 cm^{-1}. The epoxy C–O–C band is seen at 1145 cm^{-1} in the case of PS/GO. Because of hydrogen bond interactions, the C=O band is shifted at a lower frequency, causing it to overlap with the C=C band. Furthermore, carbonyl groups are concentrated around the sheet, reducing the strength of the band. The stretching vibrations of C–O in PMMA/GO were also indicated by the absorption peak at 695 cm^{-1}. These findings showed that the hydrophilicity group in PS/GO molecules was rather high. PMMA can be observed in the black line of the FTIR spectra, which shows that the monomer PMMA polymerization in this polymer mix system results in the formation of PMMA at 1732 cm^{-1}, 1453 cm^{-1}, and 1148 cm^{-1}. A sequential interpenetrating mix effectively created the blend of PS/PMMA, and composite with GO interpenetrating polymer networks.[39] The band of PMMA/GO at 2932 cm^{-1} and the band of PS/GO at 2927 cm^{-1} has shifted at 2922 cm^{-1} in the case of PS_{50}-$PMMA_{50}$/GO. All data with correlated bonds are presented in Table IV. Hydrogen bonding between PS/GO and PMMA/GO molecules may be used to explain possible microstructural alterations in blends of PS-PMMA/GO. Here, stable chemical bonding between a blended composite of PS-PMMA/GO nanoparticles may be expected based on the modifications mentioned above.[40]

XRD Analysis

XRD (Rigaku SmartLab) was recorded with $Cu_{K\alpha}$ radiation at 80 keV and a wavelength of 1.5406 Å. XRD patterns of

Table IV The shifts in the wavenumber FTIR spectra of polymer nanocomposite blends of PS-PMMA/GO

Sample	O–H stretching (cm^{-1})	C–H stretching (cm^{-1})	C=C stretching (cm^{-1})	C=O stretching (cm^{-1})	C–H bending (cm^{-1})	C–OH bending (cm^{-1})	C–O stretching (cm^{-1})	C–O bending (cm^{-1})
PS/GO	3462.32	2986.20	2206.08	2024.32	1305.63	1480.56	1160.23	942.32
PMMA/GO	3586.45	2941.80	2245.56	1724.39	1383.38	1441.64	1139.28	976.29
PS_{50}-$PMMA_{50}$/GO	3514.22	2959.36	2224.45	1703.01	1342.32	1445.13	1147.37	961.26

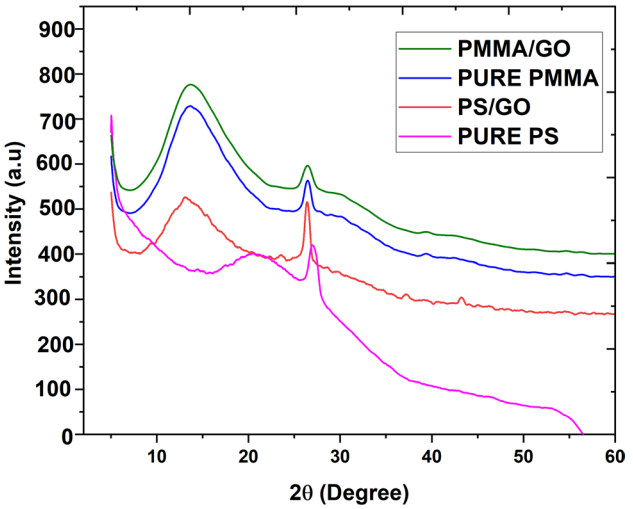

Fig. 10 XRD patterns of pure PMMA, pure PS, and PMMA/GO and PS/GO nanocomposite polymer membranes.

pure PS, pure PMMA, and PS/GO and PMMA/GO blended composite membranes are presented in Fig. 10. Sharp peaks of the graphene oxide are observed, which indicates the crystalline nature of the product. There are structural changes in polymer nanocomposites when GO nanoparticles are included. In polymer nanocomposites, including nanoparticles, the XRD pattern has sharp and diffuse peaks.[39,40]

All the blend composites show a broad and diffuse peak, which indicates the amorphous nature of the blends. XRD analyses confirm the crystalline phase transition of GO. XRD patterns of crystallized PS/GO and PMMA/GO composites from a series of composite solvents are shown in Fig. 10. The PMMA/GO diffractogram (Fig. 10) shows the characteristic scattering peak at an angle of 13.22°, which corresponds to the superposition of (1 0 0) and (2 0 0) reflections for the β phase of graphene oxide. At around 10°, the scattering from the –COOH groups in the graphite-like GO sheets causes this peak, which is usually seen at this distance. When graphene oxide is not disseminated in an aqueous solution, the XRD spectrum shows additional peaks between 10 and 45° that are typical of graphene oxide. This suggests that between two and ten overlapping GO layers may be present. As the graphene oxide is dispersed, the sheets separate, and the GO has reshaped, thus this no longer matters for making the scaffolds. In addition, the miscibility of the polymer blends has been determined by the XRD scans of the polymer blends.[38] There are separate crystal regions in the blended films of two polymers with limited compatibility, showing x-ray plots of the samples as a simple composite of properties for each polymer.

Figure 10 shows two broad peaks of PMMA/GO and pure PMMA at angles of 13.22° and 13.32°, showing that PMMA is amorphous in nature. In the first half, the side group size

Table V XRD data for pure PS, pure PMMA, and PS/GO and PMMA/GO nanocomposites

Sample name	2θ (°)	d Spacing (Å)	FWHM [°θ]	Particle size (nm)
PMMA/GO	13.22456	6.8441	2.079	40.1649
	26.26779	3.38998	20.3309	4.1908
Pure PMMA	13.32438	6.84419	0.9137	91.3936
	26.50015	3.36078	0.4074	209.26
PS/GO	13.06409	7.64604	2.7207	30.6529
	26.47055	3.36447	0.4201	202.8941
Pure PS	20.83103	8.31492	7.7933	10.6927
	27.17125	3.32736	10.2407	8.3286

corresponds to an approximately hexagonal arrangement of the molecular chains. According to van der Waals distances, the second amorphous halo may be found. The relative x-ray peak intensities allow us to evaluate the volume percentage of the graphene oxide phase generated in the samples, which has then been reported in Table V. Table V shows the 2θ and d spacing lattice characteristics for all samples. The lattice parameters observed for pure PS and pure PS/GO are 2θ (PS) = 20.83° and 2θ (PS/GO) = 13.06°, and d spacing (PS) = 8.31 Å and d spacing (PS/GO) = 7.64 Å. As the concentration of GO in the sample increases, we see a little shift of the diffraction peaks towards higher angles. This indicates that the lattice parameters of the composite samples are somewhat less than those of the pure polymer (Table V). The intensity and height of the two peaks changed as the PS level in the atmosphere increased.[39] Using this information, we may conclude that the mixes were miscible. XRD results are compatible with FTIR and DSC results. Our results show that the amount of carbon composite in GO samples is negligible compared to other carbon sources. Our analysis of the XRD patterns confirms that the crystallite size and crystallinity of the materials are decreased due to polymer composite with GO, as the full width at half maximum (FWHM) increases with the increasing composite concentration of GO in the pure polymer samples. These materials showed an amorphous nature since no clear diffraction peak could be seen in the 2θ angle range. All results of XRD patterns confirmed that PMMA/GO and PS/GO were amorphous polymers, which means PMMA and PS have an amorphous nature.[39,40]

Conclusion

The thermal and optical properties of graphene oxide dispersion in pure PS, pure PMMA, and blends of PS/PMMA were investigated, where T_g was decreased as expected by increasing the graphene oxide content compared to pure

PS, pure PMMA, and PS/PMMA blends of polymers. In the FTIR spectra of the two polymers and their mixtures, several kinds of bands were assigned. Because the blends were amorphous, XRD results revealed a wide and diffuse peak. When the PS concentration was increased, the glass transition temperature for each blend decreased. These data imply that this blend system is only miscible.[9,11,33] The slight change in the location of the edge toward the higher-frequency side of the spectrum indicates the blend's miscibility. Because of this research, the range of possible applications for graphene-based nanocomposites may be significantly expanded by chemically modifying the graphene oxide polymer interface to increase and control their physical characteristics. A single T_g peak of graphene oxide at a higher temperature, as compared to that of PS or PMMA and blends of polymers, was found for the PS/PMMA blend structure because it facilitates a miscible blend with limited free volume availability owing to the voids in the parent polymer matrix, such as PS or PMMA. Higher glass transition temperatures are necessary to activate the polymeric blends, which requires more energy. DSC showed that PMMA and PS were completely miscible in the case of polymer blend samples. PMMA and PS blends were found to be highly miscible.[14,20,22] Theoretically, Kissinger's and Augis and Bennett's equations are based on two different approaches. Augis and Bennett's method for estimating activation energy is highly dependent on thermal characteristics.

Thus, the apparent activation energy calculated from this connection must be considered. The first peak of the crystallization process was studied using all four model-dependent and model-free isokinetic and isoconversional methodologies in the system that was selected at this time. Crystallization is a phase transition from an amorphous to a crystallized state, but it is possible that this principle may be used for glass-to-amorphous transformations as well. Originally, Augis and Bennett's technique was used to determine the highest possible temperatures for crystallization to occur. For the glass transition process, the T_g is derived by summing up the beginning and the endpoints of the endothermic shift in the baseline. It is important to note that activation energy values obtained using different isoconversional approaches and particular isoconversional techniques such as Ozawa, Kissinger, Boswell, and Augis and Bennett are very similar to one another. The findings from polymer nanocomposites support the idea that the rigid amorphous fraction (RAF) cannot devitrify unless the cause of its limited mobility is removed. To release the RAF in semicrystalline polymers, inflexible crystals must be broken down. TGA data show that GO nanofillers improve the thermal properties of PS and PMMA polymers.

Acknowledgments The authors are thankful to the Applied Physics Department for providing the DSC and XRD facilities under the DST-FIST (SR/FST/PS-II/2017/20) and DST-Purse faculty scheme. The authors also acknowledge GIRDA (Vadodara, Gujarat, India) for FTIR analysis. Harsh Patel is grateful to the University Grants Commission, New Delhi, for providing Senior Research Fellowship (SRF) under NET-JRF Scheme (1217/[CSIR-UGC NET DEC. 2018]). The authors are also thankful to the Research and Consultancy Cell, M.S. University of Baroda, for providing financial assistance (RDC/Dir./2023-24/19/28).

Author Contributions Conceptualization: HP and NA. Sample preparation: HP. Methodology: HP and NA. Formal analysis and investigation: HP and NA. Writing—original draft preparation: HP and NA. Supervision: NA.

Conflict of interest The authors do not have any conflict of interest with any researcher or scientist.

References

1. L. Peeples, What the data say about wearing face masks. *Nature* 586, 186 (2020).
2. W. He, Y. Guo, H. Gao, J. Liu, Y. Yue, and J. Wang, Evaluation of regeneration processes for filtering facepiece respirators in terms of the bacteria inactivation efficiency and influences on filtration performance. *ACS Nano* 14, 13161 (2020).
3. B.S. Brown, J. Mills, and J.M. Hulse, Chemical and biological degradation of waste plastics. *Nature* 250, 161 (1974).
4. X. Sun, X. Yuan, Y. Jia, L. Feng, F. Zhu, S. Dong, J. Liu, X. Kong, H. Tian, J. Duan, Z. Ding, S. Wang, and B. Xing, Differentially charged nano plastics demonstrate distinct accumulation in *Arabidopsis thaliana*. *Nat. Nanotechnol.* 15, 755 (2020).
5. M. Raza, B. Abu-Jdayil, A.H. Al-Marzouqi, and A. Inayat, Kinetic and thermodynamic analyses of date palm surface fibers pyrolysis using Coats-Redfern method. *Renew. Energy* 183, 67 (2022).
6. S.W. Rhee, Management of used personal protective equipment and wastes related to COVID-19 in South Korea. *Waste Manag. Res.* 8, 38 (2020).
7. A. Aragaw, Surgical face masks as a potential source for microplastic pollution in the COVID-19 scenario. *Mar. Pollut. Bull.* 159, 111517 (2020).
8. A.M. Kansara, S.G. Chaudhri, and P.S. Singh, A facile one-step preparation method of recyclable superhydrophobic polypropylene membrane for oil-water separation. *RSC Adv.* 6, 61129 (2016).
9. S. Kim, X. Yang, K. Yang, H. Guo, M. Cho, Y.J. Kim, and Y. Lee, Recycling respirator masks to a high-value product: from COVID-19 prevention to highly efficient battery separator. *Chem. Eng. J.* 430, 132723 (2022).
10. L. Shao, Z. Wu, H. Duan, and T. Shaymurat, Discriminative and rapid detection of ozone realized by sensor array of Zn^{2+} doping tailored MoS_2 ultrathin nanosheets. *Sens. Actuat. B* 258, 937 (2018).
11. D. Miorandi, S. Sicari, F.D. Pellegrini, and I. Chlamtac, Internet of things: vision, applications, and research challenges. *Ad Hoc Netw.* 10, 1497 (2012).
12. H. Yuan, S.A. Aljneibi, J. Yuan, Y. Wang, H. Liu, J. Fang, C. Tang, X. Yan, H. Cai, Y. Gu, S.J. Pennycook, J. Tao, and D. Zhao, Biosensors: ZnO nanosheets abundant in oxygen vacancies derived from metal-organic frameworks for ppb-level gas sensing. *Adv. Mater.* 31, 1807161 (2019).
13. D. Zhang, Z. Yang, P. Li, M. Pang, and Q. Xue, Flexible self powered high-performance ammonia sensor based on Au-decorated

$MoSe_2$ nanofowers driven by single-layer $MOSe_2$-flake piezoelectric nanogenerator. *Nano Energy* 65, 103974 (2019).
14. H. Yue, A.M. Soleimanpour, and A.H. Jayatissa, Low resistive aluminum-doped nanocrystalline zinc oxide for reducing gas sensor application via sol-gel process. *Sens. Actuat. B* 204, 310 (2014).
15. H. Liu, M. Li, O. Voznyy, L. Hu, Q. Fu, D. Zhou, Z. Xia, E.H. Sargent, and J. Tang, Physically flexible, rapid-response gas sensor based on colloidal quantum dot solids. *Adv. Mater.* 26, 2718 (2014).
16. W. Gao, S. Emaminejad, H.Y. Nyein, K. Chen, A. Peck, H.M. Fahad, H. Ota, H. Shiraki, and D. Kiriya, Fully integrated wearable sensor arrays for multiplexed in situ perspiration analysis. *Nature* 529, 509 (2016).
17. S. Rehman, S. Rafiq, N. Muhammad, M. Irfan, S.U. Zaman, F. Jamil, S. Saqib, A. Mukhtar, K.S. Khoo, M. Mubashir, P.L. Show, Surface tuning of silica by deep eutectic solvent to synthesize biomass derived based membranes for gas separation to enhance the circular bioeconomy. *Fuel* 31, 122355 (2022).
18. Q. Sun, Z. Wu, Y. Cao, J. Guo, M. Long, and H. Duan, Chemiresistive sensor arrays based on noncovalently functionalized multiwalled carbon nanotubes for ozone detection. *Sensor Actuat. B* 297, 126689 (2019).
19. S. Vyazovkin, Kissinger method in kinetics of materials: things to beware and be aware of. *Molecules* 25(12), 2813 (2020).
20. S. Chen, R. Yuan, Y. Chai, and F. Hu, Electrochemical sensing of hydrogen peroxide using metal nanoparticles: a review. *Microchim. Acta* 180, 15 (2013).
21. W. Chen, S. Cai, Q. Ren, W. Wen, and Y. Zhao, Recent advances in electrochemical sensing for hydrogen peroxide: a review. *Analyst* 137, 49 (2011).
22. E.I. Muller, C.C. Muller, J.P. Souza, A.L.H. Muller, M.S.P. Enders, M. Doneda, A.C. Frohlich, G.D. Top, and K.F. Anschau, Green microwave-assisted wet digestion method of carbohydrate-rich foods with hydrogen peroxide using single reaction chamber and further elemental determination using ICP-OES and ICP-MS. *Microchem. J.* 134, 257 (2017).
23. J.M. Rosa, E.B.A. Tambourgi, and J.C. Santana, Dyeing of cotton with reactive dyestuffs: the continuous reuse of textile wastewater effluent treated by ultraviolet/hydrogen peroxide homogeneous photocatalysis. *J. Clean. Prod.* 90, 60 (2015).
24. G. Liu, F. Xiangli, W. Wei, S. Liu, and W. Jin, Improved performance of PDMS/ceramic composite pervaporation membranes by ZSM-5 homogeneously dispersed in PDMS via a surface graft/coating approach. *Chem. Eng. J.* 174, 495 (2011).
25. R. Banavath, R. Srivastava, and P. Bhargava, Nanoporous cobalt hexacyanoferrate nanospheres for screen-printed H_2O_2 sensors. *ACS Appl. Nano Mater.* 4, 5564 (2021).
26. Y.A. Chiao, H. Zhang, M. Sweetwyne, J. Whitson, and P. Rabinovitch, Late-life restoration of mitochondrial function reverses cardiac dysfunction in old mice. *Life* 9, e55513 (2020).
27. W. Zhang, Z. Wu, J. Hu, Y. Cao, J. Guo, M. Long, H. Duan, and D. Jia, Flexible chemiresistive sensor of polyaniline coated filter paper prepared by spraying for fast and non-contact detection of nitroaromatic explosives. *Sens. Actuat. B* 304, 1272331 (2020).
28. Z. Wu, C. Zhou, B. Zu, Y. Li, and X. Dou, Contactless and rapid discrimination of improvised explosives realized by Mn^{2+} doping tailored ZnS nanocrystals. *Adv. Funct. Mater.* 26, 4578 (2016).
29. M. Volder, S.H. Tawfck, R.H. Baughman, and A.J. Hart, Carbon nanotubes: present and future commercial applications. *Science* 339, 535 (2013).
30. M.E. Franke, T.J. Koplin, and U. Simon, Metal and metal oxide nanoparticles in chemiresistors: does the nanoscale matter? *Small* 2, 36 (2010).
31. S. Bai, C. Sun, P. Wan, C. Wang, R. Luo, Y. Li, J. Liu, and X. Sun, Transparent conducting films of hierarchically nanostructured polyaniline networks on flexible substrates for high-performance gas sensors. *Small* 11, 306 (2015).
32. D. Zhang, C. Jiang, P. Li, and Y. Sun, Layer-by-layer self-assembly of Co_3O_4 nanorod-decorated MoS2 nanosheet-based nanocomposite toward high-performance ammonia detection. *ACS Appl. Mater. Interfaces* 9, 6462 (2017).
33. W. Zhang, X. Zhang, Z. Wu, K. Abdurahman, and D. Jia, Mechanical, electromagnetic shielding and gas sensing properties of flexible cotton fiber/polyaniline composites. *Compos. Sci. Technol.* 188, 107966 (2019).
34. C. Fang, D. Cen, Y. Wang, Y. Wu, and G. Han, Zns@ZIF-8 core-shell nanoparticles incorporated with ICG and TPZ to enable H_2S-amplifed synergistic therapy. *Theranostics* 10, 7671 (2020).
35. G.L. Jadav and P.S. Singh, Synthesis of novel silica-polyamide nanocomposite membrane with enhanced properties. *J. Membr. Sci.* 328, 557 (2009).
36. R. Zhang, Q. Chen, Z. Zhen, X. Jiang, M. Zhong, and H. Zhu, Cellulose-templated graphene monoliths with anisotropic mechanical, thermal, and electrical properties. *ACS Appl. Mater. Int.* 7, 19145 (2015).
37. S. Marinello, F. Lolli, R. Gamberini, and B. Rimini, A second life for cigarette butts? A review of recycling solutions. *J. Hazard. Mater.* 384, 121245 (2019).
38. F. Thuemmler and V. Hettrich, Schmidt, properties and applications of cellulose acetate, *Macromol Symposia*. (Wiley, 2008).
39. R. Li, X. Tian, M. Wei, A.A. Dong, X. Pan, Y. He, and X. Song, Flexible pressure sensor based on cigarette filter and highly conductive MXene sheets. *Compos. Commun.* 27, 100889 (2021).
40. J. Li, Y. Liu, J. Zhang, X. Liang, and H. Duan, Density functional theory study of the adsorption of hydrogen atoms on Cu_2X (X=3d) clusters. *Chem. Phys. Lett.* 651, 137 (2016).

Authors and Affiliations

Harsh D. Patel[1] · Naveen K. Acharya[1]

✉ Naveen K. Acharya
sarnavee@gmail.com

[1] Applied Physics Department, Faculty of Technology and Engineering, The M.S. University of Baroda, Vadodara 390 001, India